Mon. Not. R. Astron. Soc. **415,** 1228–1239 (2011) doi:10.1111/j.1365-2966.2011.18748.x

Numerical parameter survey of non-radiative black hole accretion: flow structure and variability of the rotation measure

Bijia Pang,[1⋆] Ue-Li Pen,[2⋆] Christopher D. Matzner,[3⋆] Stephen R. Green[4⋆] and Matthias Liebendörfer[5⋆]

[1]*Department of Physics, University of Toronto, M5S 1A7, Canada*
[2]*Canadian Institute for Theoretical Astrophysics, University of Toronto, M5S 3H8, Canada*
[3]*Department of Astronomy and Astrophysics, University of Toronto, M5S 3H8, Canada*
[4]*Department of Physics, University of Chicago, 5640 South Ellis Avenue, Chicago, IL 60637, USA*
[5]*Physics Department, University of Basel, Klingelbergstrasse 82, CH-4056 Basel, Switzerland*

Accepted 2011 March 18. Received 2011 March 18; in original form 2010 November 14

ABSTRACT

We conduct a survey of numerical simulations to probe the structure and appearance of non-radiative black hole accretion flows like the supermassive black hole at the Galactic Centre. We find a generic set of solutions, and make specific predictions for currently feasible rotation measure (RM) observations, which are accessible to current instruments including the Expanded Very Large Array (EVLA), Giant Metrewave Radio Telescope (GMRT) and Atacama Large Millimeter Array (ALMA). The slow time variability of the RM is a key quantitative signature of this accretion flow. The time variability of RM can be used to quantitatively measure the nature of the accretion flow, and to differentiate models. Sensitive measurements of RM can be achieved using RM synthesis or using pulsars.

Our energy conserving ideal magnetohydrodynamical simulations, which achieve high dynamical range by means of a deformed-mesh algorithm, stretch from several Bondi radii to about one-thousandth of that radius, and continue for tens of Bondi times. Magnetized flows which lack outward convection possess density slopes around -1, almost independent of physical parameters, and are more consistent with observational constraints than are strongly convective flows. We observe no tendency for the flows to become rotationally supported in their centres, or to develop steady outflow.

We support these conclusions with formulae which encapsulate our findings in terms of physical and numerical parameters. We discuss the relation of these solutions to other approaches. The main potential uncertainties are the validity of ideal magnetohydrodynamic and the absence of a fully relativistic inner boundary condition. The RM variability predictions are testable with current and future telescopes.

Key words: accretion, accretion discs – black hole physics – MHD.

1 INTRODUCTION

The radio source Sgr A* at the Galactic Centre (GC) is now accepted to be a supermassive black hole ($M_{\rm BH} \simeq 4.3 \times 10^6\,{\rm M}_\odot$; Gillessen et al. 2009), accreting hot gas from its environment ($n_{\rm e} \simeq 130\,{\rm cm}^{-3}, k_{\rm B}T \simeq 2\,{\rm keV}$ at 1 arcsec; Baganoff et al. 2003). Interest in the Sgr A* accretion flow is stimulated by its remarkably low luminosity, by its similarity to other low-luminosity AGN, by circumstantial evidence for past episodes of bright X-ray emission (Revnivtsev et al. 2004, but see Yusef-Zadeh et al. 2007) and nearby star formation (Levin & Beloborodov 2003), and, foremost, by its status as an outstanding physical puzzle.

Supermassive black holes are enigmatic in many respects; for the GC black hole (GCBH) the enigma is sharpened by a wealth of observational constraints, which permit detailed, sensitive and spatially resolved studies of its accretion dynamics. Within a naïve model such as Bondi flow, matter would flow inwards at the dynamical rate from its gravitational sphere of influence, which at $\sim$1 arcsec is resolved by *Chandra*. Converted to radiation with an efficiency ηc^2, the resulting luminosity would exceed what is actually observed by a factor $\sim 10^5(\eta/0.1)$. This wide discrepancy between expectation and observation has stimulated numerous theoretical explanations, including convection (Narayan, Igumenshchev

⋆E-mail: bpang@physics.utoronto.ca (BP); pen@cita.utoronto.ca (U-LP); matzner@cita.utoronto.ca (CDM); srgreen@uchicago.edu (SRG); matthias.liebendoerfer@unibas.ch (ML)

& Abramowicz 2000; Quataert & Gruzinov 2000b), outflow (Blandford & Begelman 1999), domination by individual stars' winds (Loeb 2004) and conduction (Tanaka & Menou 2006; Johnson & Quataert 2007; Sharma, Quataert & Stone 2008; Shcherbakov & Baganoff 2010).

1.1 Constraining the accretion flow

Because many of its parameters are uncertain, the central density and accretion rate of the GCBH flow are not strongly constrained by the its emission spectrum (Quataert & Narayan 1999); the most stringent constraints come from observations of the rotation measure (RM; Quataert & Gruzinov 2000a), now known to be roughly $-5.4 \times 10^5\,\mathrm{rad\,m^{-1}}$ (Marrone et al. 2007). Interpreting this as arising within a quasi-spherical flow with magnetic fields in rough equipartition with gas pressure, and adopting the typical assumption that magnetic fields do not reverse rapidly, we derive a gas density $n_\mathrm{H} \sim 10^{5.5}\,\mathrm{cm^{-3}}(R_\mathrm{S}/R_\mathrm{rel})^{1/2}$ at the radius R_rel which dominates the RM integral, namely where electrons become relativistic; see Appendix A for more detail. If this radius is about 10^2 Schwarzschild radii ($10^2 R_\mathrm{S}$), as in the spectral models of Quataert & Narayan (1999), then a comparison between this density and conditions at the Bondi radius $R_\mathrm{B} \simeq 0.053\,\mathrm{pc}$ indicates a density power law $\rho \propto r^{-k}$ with $k = 1.1$–1.3; the derived value is rather insensitive to the black hole mass, the degree of equipartition and the precise radius at which electrons become relativistic. (If rapid conduction causes electrons to be non-relativistic at all radii, the implied slope falls to 0.8.)

An independent but weak constraint on k comes from recent multiwavelength observations of flares in the emission from Sgr A*. Yusef-Zadeh et al. (2009a) favour an interpretation in which these flares originate within regions in which electrons have been transiently heated and accelerated; using equipartition arguments they estimate a magnetic field strength $B \sim 13$–$15\,\mathrm{G}$ at 4–10 Schwarzschild radii, implying a total pressure $P > 20\,\mathrm{dyn\,cm^{-2}}$ at those radii. Because $P \propto r^{-(k+1)}$, a comparison to the conditions at R_B requires $k > 0.6$–0.8. This constraint could be violated if the emitting regions were sufficiently overpressured relative to the surrounding gas; however the subsonic rate of expansion inferred by Yusef-Zadeh et al. (2009b) suggests this is not the case.

The density power law k is an important diagnostic, both because it allows one to estimate the mass accretion rate on to the black hole, and because k takes definite values within proposed classes of accretion flows. Bondi (1952) accretion and advection-dominated accretion flows (ADAFs; Narayan & Yi 1994), in which gas undergoes a modified free fall, imply $k = 3/2$ and have long been ruled out (Agol 2000) by limits on the RM (Bower et al. 1999). Convection-dominated accretion flows (CDAFs; Narayan et al. 2000; Quataert & Gruzinov 2000b) and related flows like convection-dominated Bondi flows (CDBFs; Igumenshchev & Narayan 2002), in which convection carries a finite outward luminosity, all have $k = 1/2$ outside some small radius: otherwise, convection becomes supersonic (Gruzinov 2001).

Three classes of flows are known to have intermediate values, $1/2 < k < 3/2$, as suggested by the observations. One of these is the advection-dominated inflow–outflow solutions (ADIOS; Blandford & Begelman 1999), in which mass is lost via a wind from all radii within a rotating ADAF; however these flows appear to require that low-angular-momentum material has been removed from the axis. Another is a class of conductive flows, in which heat is carried outward by electrons and stifles accretion at large radii (Johnson & Quataert 2007). The third consists of flows which lack any significant outward convective or conductive luminosity (Gruzinov 2001), but are nevertheless hydrostatic rather than infalling; this behaviour is seen within some numerical simulations in which *magnetized* gas is accreted, such as those of Igumenshchev, Narayan & Abramowicz (2003) and Pen, Matzner & Wong (2003b), who termed the flow 'magnetically frustrated convection'.

We are concerned with the last flow class, as it is physically simple, realizable within simulations, and consistent with observational constraints. Whether it is physically relevant depends on the strength of conduction in the accretion flow, a question we return to in Section 5. Although it is of interest, previous simulations do not suffice to make any quantitative comparisons between it and the Sgr A* accretion flow. Igumenshchev et al. (2003) have already discussed several shortcomings which afflicted prior numerical work, such as (1) a lack of energy conservation during magnetic reconnection and (2) simulation durations too short to capture steady states or secular trends. There are a number of other roadblocks: (3) *dynamical range*: R_B is 10^5 Schwarzschild radii, but the largest simulations yet done have only a factor of $\sim 10^2$ separating their inner and outer boundaries; (4) *resolution*: numerical solutions are rarely close enough to the continuum limit to allow turbulent phenomena to be predicted with confidence; (5) *outer boundary conditions*: although matter is presumably fed into the accretion flow by stellar winds from the nuclear star cluster (Genzel et al. 2003), the flow structure and magnetization of this gas is not well constrained; (6) *inner boundary conditions*: the hole interacts with the flow in a manner which is not fully characterized, and which is likely to dominate the energetics; (7) *mass injection*: stars within R_B produce fresh wind material, which have the potential to affect the final solution (Loeb 2004) and (8) *plasma physics*: close to the black hole, the flow is only weakly collisional, leading to effects such as anisotropic pressure and conduction, which may alter the nature of fluid instabilities and the character of heat transport (Sharma et al. 2008). Potential deviations from ideal magnetohydrodynamic (MHD) become stronger as one approaches the event horizon, and are discussed further in Section 5.

In this paper we describe a numerical parameter survey designed to partially overcome difficulties (1)–(5) in the above list, while making an educated guess regarding (7) and leaving (6) and (8) to future work. Specifically, we conduct 3D, explicitly energy conserving simulations to the point of saturation – often tens of dynamical times at R_B. We vary the dynamical range and resolution in order to gather information about the astrophysical limits of these parameters, although they lie beyond our numerical reach. We push numerical outer boundaries far enough from R_B to minimize their effect on the flow, and we vary the conditions exterior to R_B in order to gauge the importance of magnetization and rotation in the exterior fluid. Our simulations obey ideal MHD, but are viscous and resistive on the grid scale for numerical reasons; we make no attempt to capture non-ideal plasma effects. We do not account for stellar mass injection within the simulation volume. Our gravity is purely Newtonian, and at its base we have a region of accretion and reconnection rather than a black hole (although we are currently pursuing relativistic simulations to overcome this limitation). Our numerical approach is described more thoroughly below.

By varying the conditions of gas outside R_B and by varying the allocation of grid zones within R_B we are able to disentangle, to some degree, physical and numerical factors within our results. We also compute integrated quantities related to the value and time evolution of RM, and draw conclusions regarding the importance of RM(t) as a powerful discriminant between physical models.

We reiterate that our simulations have two simplifications which could substantially change the behaviour. (1) Our black hole boundary condition is Newtonian. Since the deepest potential dominates the dynamics and energy of the flow, a change in this assumption might alter the solution. (2) We assume ideal MHD to hold. As one approaches the black hole, the Coulomb collision rate is insufficient to guarantee local thermodynamic equilibrium. Plasmas can thermalize through other plasma processes, but if these fail, strong non-ideal effects could dominate and lead to rapid conduction. These effects are both strongest at small radii, potentially modifying the extrapolation to the actual physical parameters. We address these issues in more detail in Section 5.

2 SIMULATION

2.1 Physical setup and dimensionless physical parameters

We wish our simulations to be reasonably realistic with regard to the material which accretes on to the black hole, but also easily described by a few physical and numerical parameters. We therefore do not treat the propagation and shocking of individual stellar winds or turbulent motions, but take the external medium to be initially of constant density ρ_0 and adiabatic sound speed c_{s0}, and imbued with a characteristic magnetic field B_0 and characteristic rotational angular momentum j_0 (but no other initial velocity). A Keplerian gravity field $-GM/r^2$ accelerates material towards a central 'black hole' of mass M surrounded by a central accretion zone. The Bondi accretion radius is therefore

$$R_{\rm B} = \frac{GM}{c_{\rm s0}^2}. \tag{1}$$

We adopt the Bondi time $t_{\rm B} = R_{\rm B}/c_{\rm s0}$ as our basic time unit; this is 100 yr for the adopted conditions at Sgr A*. All of the initial flow quantities will evolve as a result of this during the course of the simulation, and we run for many Bondi times in order to allow the accretion flow to settle into a final state quite different from our initial conditions. From the above dimensional quantities we define several dimensionless physical parameters.

The adiabatic index is $\gamma = 5/3$; the initial plasma-β parameter, or ratio of gas to magnetic pressure, is

$$\beta_0 = \frac{8\pi\gamma\rho_0 c_{\rm s0}^2}{B_0^2}; \tag{2}$$

we consider models with $\beta_0 = (1, 10, 100, 1000, \infty)$ to capture a wide range of plausible magnetizations. In our main sequence of simulations, we adopt a uniform magnetic field $\boldsymbol{B}_0$ with the angle θ_{Bj} between $\boldsymbol{B}_0$ and j taking values 45°, 63° or 90°.[1]

The initial velocity field is $\boldsymbol{v}_0 = (\boldsymbol{j}_0 \times \hat{\boldsymbol{r}})/r$, where $\boldsymbol{r}$ is the separation from the black hole. The specific vector angular momentum is thus $\boldsymbol{j}_0$ at the rotational equator, with solid-body rotation on spherical shells away from the equator. A dimensionless rotation parameter is therefore

$$\frac{R_{\rm K}}{R_{\rm B}} = \left(\frac{j_0 c_{\rm s}}{GM}\right)^2; \tag{3}$$

here $R_{\rm K} = j_0^2/(GM)$ is the Keplerian circularization radius of the equatorial inflow. (Our flows never do circularize at $R_{\rm K}$, both because angular momentum transport alters the distribution of j, and because gas pressure can never be neglected.)

We impose mass accretion and magnetic field reconnection within a zone of characteristic radius $R_{\rm in}$, described below, which introduces the dynamic range parameter $R_{\rm B}/R_{\rm in}$. Because it sets the separation between small and large scales and the maximum depth of the potential well, this ratio has a strong influence on flow properties. One of our goals is to test how well the flow quantities at high dynamic range can be predicted from simulations done at lower dynamic range, as the dynamic range appropriate to Sgr A* is beyond what we can simulate.

2.2 Grid setup and numerical parameters

We employ a fixed, variable-spacing Cartesian mesh in which the grid spacing increases with distance away from the black hole. To simplify our boundary conditions, we hold the spacing fixed within the inner accretion zone and near the outer boundary. The total box size is 4000^3 in units of the minimum grid spacing; however this is achieved within a numerical grid of only 300^3–600^3 zones. Our grid geometry allows for a large number of long-duration runs to be performed at respectable values of the dynamic range, while avoiding coordinate singularities and resolution boundaries. These advantages come at the cost of introducing an anisotropy into the grid resolution; however we have tested the code for conservation of angular momentum and preservation of magnetosonic waves, and found it to be comparable in accuracy to fixed-grid codes with the same resolution. Our grid expansion factor $s = \delta\,{\rm d}x_i/{\rm d}x_i$ takes one value for $x_i < R_{\rm B}$ and another, larger value for $x_i > R_{\rm B}$; this allows us to devote most of our computational effort to the accretion region of interest, while also pushing the (periodic) outer boundary conditions far away from this region. The inner expansion factor $s_{\rm in}$ is therefore an important numerical parameter, related to both the grid's resolution and its anisotropy where we care most about the flow.

Within our inner accretion region, magnetic fields are reconnected (relaxed to the vacuum solution consistent with the external field; see Appendix B) and mass and heat are adjusted (invariably, removed) so that the sound speed and Alfvén velocity both match the Keplerian velocity at $R_{\rm B}$. The accretion zone is a cube, whose width we hold fixed at 15 in units of the local (uniform) grid separation, so we define $R_{\rm in} = 7.5\,{\rm d}x_{\rm min}$ (but note the volume of this region is equivalent to a sphere of radius $9.3\,{\rm d}x_{\rm min}$.) We consider it too costly to vary the numerical parameter $R_{\rm in}/{\rm d}x_{\rm min}$.

Our grid geometry imposes a local dimensionless resolution parameter:

$$\Re \equiv \frac{r}{\max_i({\rm d}x_i)} \tag{4}$$

(the maximum being over coordinate directions), which depends both on radius and on angle within the simulation volume. At the inner boundary $\Re \simeq 7.5$–9.3, $\Re$ increases to nearly $s_{\rm in}^{-1} \simeq 10^2$ at $R_{\rm B}$, then decreases towards $s_{\rm out}^{-1}$ in the exterior region. In Section 3 we report the effective resolution at the Bondi radius, $\Re_{\rm B} = \Re(R_{\rm B})$, along with our results.

2.3 Computational implementation

Our simulations were performed on the Canadian Institute for Theoretical Astrophysics Sunnyvale cluster: 200 Dell PE1950 compute nodes; each node contains two quad core Intel(R) Xeon(R) E5310

[1] We also investigated scenarios with Gaussian random field components, in which the dominant wavelengths were some multiple of $R_{\rm B}$; however we abandoned these, as such fields decay on a Alfvén crossing time, confounding our attempts to quantify the accretion flow, and we did not wish to add a turbulent driver to maintain steady state.

Table 1. Simulations described in this paper. Columns: run number; maximum resolution relative to the Bondi radius; radial dynamic range within R_B; grid expansion factor within R_B; effective resolution at R_B; magnetization parameter; rotation parameter; range of simulation times over which flow properties were measured; angle between magnetic field and rotation axis; mean mass accretion rate and typical density power-law slope ($\rho \propto r^{-k}$).

Run	$\frac{R_B}{dx_{min}}$	$\frac{R_B}{R_{in}}$	$1+s_{in}$	$\Re_B$	β_0	$\frac{R_K}{R_B}$	$\frac{t_{sim}}{t_B}$	θ_{Bj}	$\frac{\dot{M}}{\dot{M}_{Bondi}}$	k_{eff} [a]
1	500	67	1.023	40.15	∞	0	8	N/A	1.02	1.5047
2	250	33	1.013	59.29	∞	0	3	N/A	1.10	1.5273
3	125	17	1.013	48.11	100	0	6–20	45°	0.49	1.2482
4	250	33	1.013	59.29	100	0	6–20	45°	0.31	1.1650
5	500	67	1.023	40.15	100	0	6–20	45°	0.22	1.1399
6	1000	133	1.0315	30.82	100	0	6–10	45°	0.16	1.1253
7	250	33	1.013	59.29	1	0	6–20	45°	0.15	0.9574
8	250	33	1.013	59.29	10	0	6–20	45°	0.26	1.1147
9	250	33	1.013	59.29	1000	0	6–20	45°	0.40	1.2379
10	250	33	1.013	59.29	100	0.1	6–20	45°	0.289	1.1450
11	250	33	1.013	59.29	100	0.5	6–20	45°	0.286	1.1420
12	250	33	1.013	59.29	100	1.0	6–20	45°	0.31	1.1650
13[b]	62.5	33	1.06	14.24	100	0	6–20	45°	0.30	1.1557
14[c]	125	33	1.037	28.94	100	0	6–20	45°	0.33	1.1829
15	250	33	1.013	59.29	∞	0.1	6–20	45°	0.615	1.3610
16	250	33	1.013	59.29	∞	0.5	6–20	45°	0.621	1.3637
17	250	33	1.013	59.29	∞	1.0	6–20	45°	0.759	1.4211
18	250	33	1.013	59.29	1000	0.1	6-20	45°	0.400	1.2379
19	250	33	1.013	59.29	1000	0.1	6–20	90°	0.469	1.2835
20	250	33	1.013	59.29	100	0.1	6–20	90°	0.300	1.1557
21	250	33	1.013	59.29	10	0.1	6–20	90°	0.233	1.0834
22	250	33	1.013	59.29	1	0.1	6–20	90°	0.188	1.0220
23	250	33	1.013	59.29	100	0	6–20	90°	0.340	1.1915
24	500	67	1.0315	31.65	100	0.1	6–20	63°	0.18	1.2434
25[d]	1000	58.9	1.015	64	100	0.1	6–20	63°	0.19	1.0925
26[e]	8000	117	1.00185	515	100	0.1	21.1465	63°	0.11	1.0365

[a]Values are taken from equation (5); [b]case of 75^3 grid resolution; [c]case of 150^3 grid resolution; [d]case of 600^3 grid resolution; [e]case of 4680^3 grid resolution.

@ 1.60-GHz processors, 4GB of RAM and 2 gigE network interfaces. The code (Pen, Arras & Wong 2003a) is a second-order accurate (in space and time) high-resolution total variation diminishing MHD parallelized code. Kinetic, thermal and magnetic energy are conserved and divergent of magnetic field was kept to zero by flux-constrained transport. There is no explicit magnetic and viscous dissipation in the code except on the grid scale. We used an MPI version (Kaeppeli et al. 2009), and 216 CPU cores were used to compute a 300^3 box, using Open Multi-Processing (OpenMP) with 8 cores per node. The 600^3 simulation was performed on the SciNet cluster using 1000 cores over 125 nodes.[2]

In 2010 December we were able to perform the largest black hole accretion simulation using 17 576 CPU cores on the SciNet cluster. We started with the $20\,t_B$ data from 1000 CPU cores simulation at 600^3 resolution. In order to fit the node decomposition, this was truncated to 585^3 grid cells. 30 700 time-steps for $0.06\,t_B$ were spent for 585^3 box on 1000 CPU cores, with the smallest grid spacing $dx = 1$; 7600 time-steps for $0.08\,t_B$ were spent for 1170^3 box on 1000 CPU cores, with the smallest grid $dx = 0.5$; 3600 time-steps for $0.006\,t_B$ were spent for 2340^3 box on 5832 CPU cores, with the smallest grid $dx = 0.25$; 3000 time-steps for $0.0006\,t_B$ were spent for 4680^3 box on 17 576 CPU cores, with the smallest grid $dx = 0.125$.

While this last high-resolution simulation did not run for long enough to demonstrate a stationary behaviour, it is nevertheless consistent with no substantial change as one increases resolution.

A parallel effort to implement the code on economic graphics processing units is in progress, which will allow larger and longer simulations in the future (Pang, Pen & Perrone 2010).

3 SIMULATIONS AND RESULTS

Our suite of simulations is described in Table 1, along with some selected results. We independently varied the magnetization, rotation and dynamic range of the flow, as well as the effective resolution at R_B. In order to suppress the lingering effects of our initial conditions, we ran each simulation for long enough that a total mass equivalent to all the matter initially within R_B was eventually accreted, before assessing the flow structure. Because most of our runs exhibited a significant suppression of the mass accretion rate $\dot{M}$ relative to the Bondi value, this constraint required us to simulate for many t_B (typically $20t_B$). This requirement put strenuous constraints on our simulations (each of which required $\sim$3 weeks to complete), and will be a serious limitation on any future simulations performed at higher dynamic range.

3.1 Character of saturated accretion flows

Fig. 1 shows the 2D slices for the simulation of 600^3 box at 15 Bondi times (case 25).[3] The remaining figures are all based on case 10, which is most representative of the whole set of simulations. Figs 2

[2] http://www.scinet.utoronto.ca/

[3] Movies are also available in various formats at http://www.cita.utoronto.ca/pen/MFAF/blackhole_movie/index.html

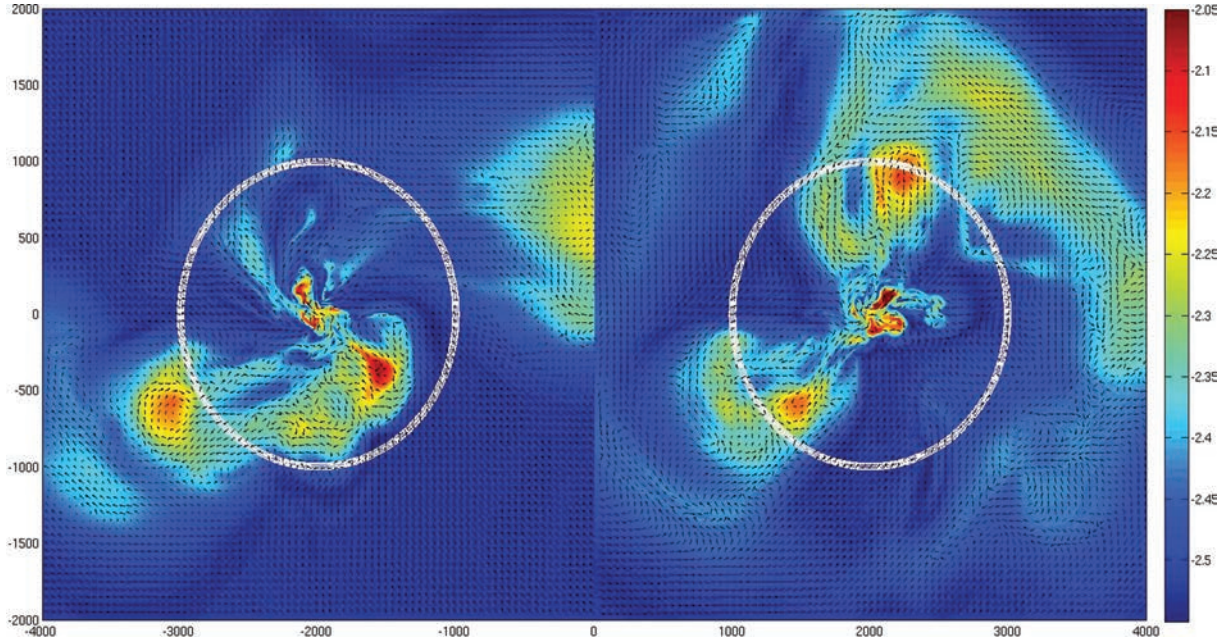

Figure 1. 2D slice of the simulation for 600^3 box at 15 Bondi times. Colour represents the entropy, and arrows represent the magnetic field vector. The right-hand panel is the equatorial plane (*yz*), while the left-hand panel a perpendicular slice (*xy*). White circles represent the Bondi radius ($r_B = 1000$). The fluid is slowly moving, in a state of magnetically frustrated convection. A movie of this flow is available as Supporting Information with electronic version of this article (see Appendix C for a description).

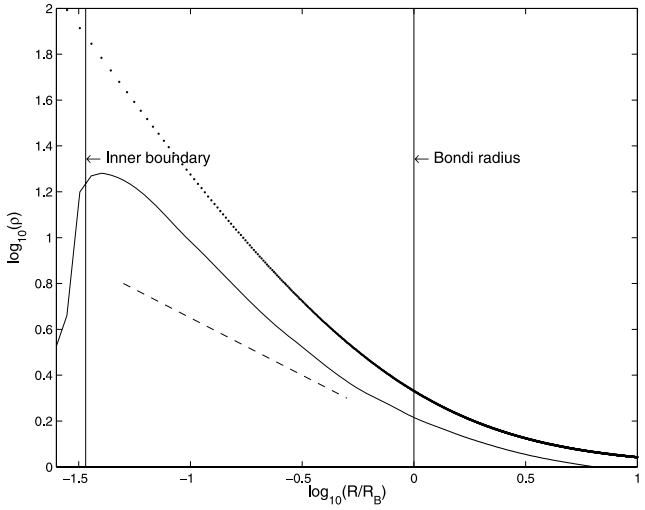

Figure 2. Density versus radius. The dotted line represents the density profile for the Bondi solution, which is the steepest plausible slope at $k = 1.5$. The dashed line represents the density scaling for CDAF solution, which is the shallowest proposed slope with $k = 0.5$. The solid line is the density profile from one of our simulations, which is intermediate to the two.

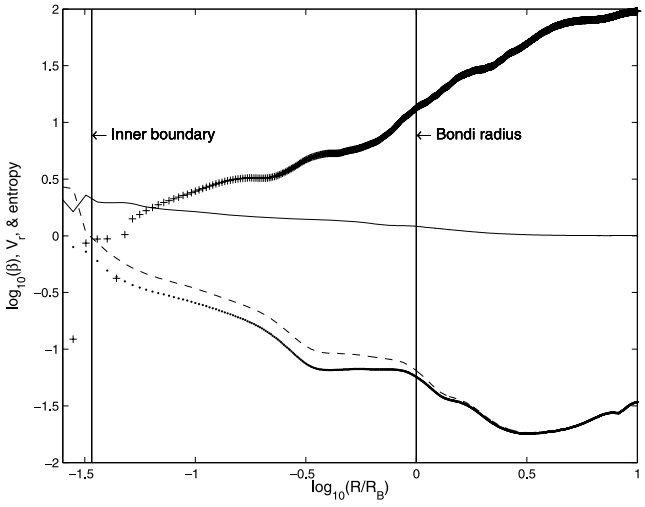

Figure 3. $\log(\beta)$, entropy and radial velocity versus radius. The dashed line v_r/c_s represents the radial velocity in units of Mach number. The dots v_r/c_{ms} represent the radial velocity in units of magnetosonic Mach number. The solid line is the entropy, and we see the entropy inversion which leads to the slow, magnetically frustrated convection. Inside the inner boundary, the sound speed is lowered, leading to the lower entropy. The '+' symbols are the magnetic field strength β.

and 3 display the spherically averaged properties, Fig. 2 shows the spherically averaged density of the run; Fig. 3 shows the spherically averaged radial velocity, β and entropy (normalized to the initial entropy). The entropy inversion is clearly visible, which leads to the slow, magnetically frustrated convection.

We draw several general conclusions from the runs listed in Table 1.

(i) In the presence of magnetic fields, the flow develops a superadiabatic temperature gradient and flattens to $k \sim 1$. Gas pressure remains the dominant source of support at all radii, although magnetic forces are always significant at the inner radius.

(ii) Mass accretion diminishes with increasing dynamic range, taking values $\dot{M} \simeq (2\text{–}4)\dot{M}_B(R_{in}/R_B)^{3/2-k}$.

(iii) Even significant rotation at the Bondi radius has only a minor impact on the mass accretion rate, as the flows do not develop rotationally supported inner regions.

(iv) Our results depend only weakly on the effective resolution $\Re_B$.

(v) In the absence of magnetic fields and rotation, a Bondi flow develops. (Pen et al. 2003b further demonstrated a reversion to Bondi inflow if magnetic fields are suddenly eliminated; we have not repeated this experiment.)

3.1.1 Lack of rotational support

The non-rotating character of the flow casts some doubt on models which depend on equatorial inflow and axial outflow. Our non-relativistic simulations cannot rule out an axial outflow from a spinning black hole, but they certainly show no tendency to develop rotational support in their inner regions, even after many tens of dynamical times. In a rotating run, angular momentum is important at first, in preventing the accretion of matter from the equator. Axial, low-j material does accrete, but some of it shocks and drives an *outflow* along the equator (as reported by Pen et al. 2003b and Proga & Begelman 2003). After a few $t_{\rm B}$ this quadrupolar flow disappears, leaving behind the nearly hydrostatic, slowly rotating envelope which persists for our entire simulation time, i.e. tens of $t_{\rm B}$. We attribute the persistence of this rotational profile to magnetic braking, as the Alfvén crossing time of the envelope is always shorter than its accretion time. Magnetic fields thus play a role here which is rather different than in simulations which start from a rotating torus, where the magnetorotational instability is the controlling phenomenon; the critical distinction is the presence of low-angular-momentum gas.

Unlike compact object discs, which accrete high-angular-momentum material and are guaranteed to cool in a fraction of their viscous time, the GCBH feeds upon low-angular-momentum matter, and its accretion envelope cannot cool. For both of these reasons, it is not surprising to discover a thick, slowly rotating accretion envelope rather than a thin accretion disc. We stress that global simulations, which resolve the Bondi radius and beyond and continue for many dynamical times, are required to capture the physical processes which determine the nature of the flow.

3.1.2 Dependence on parameters; Richardson extrapolation

We now investigate whether our results for the accretion rate can be distilled into a single, approximate expression. It is clear from the results in Table 1 that rotation affects the accretion rate in a non-monotonic fashion. However, as we have just noted that rotation plays a minor role in our final results, we are justified in fitting only the non-rotating runs. Rather than $\dot{M}/\dot{M}_{\rm Bondi}$ we fit an effective density slope $k_{\rm eff}$ defined by

$$\frac{\dot{M}}{\dot{M}_{\rm Bondi}} = \left(\frac{R_{\rm in}}{R_{\rm B}}\right)^{3/2-k_{\rm eff}}. \tag{5}$$

There are four major variables: the magnitude of the ambient magnetic field (β_0); the radial dynamical range ($R_{\rm B}/R_{\rm in}$) and the resolution of the Bondi scale ($\Re_{\rm B}$). Our fit is

$$k_{\rm eff} = 1.50 - 0.56\beta_0^{-0.098} + 6.51\left(\frac{R_{\rm B}}{R_{\rm in}}\right)^{-1.4} - 0.11\Re_{\rm B}^{-0.48}; \tag{6}$$

all seven numerical coefficients and exponents were optimized against the 25 runs in Table 1. The form of equation (6) is significantly better than others we tested, including those involving $\log(R_{\rm B}/R_{\rm in})$ and $\log(\Re_{\rm B})$. It predicts the entries in Table 1 to within an rms error of only 0.017.

Somewhat unexpectedly, this non-linear fit to our simulation output recovers the Bondi solution in the continuum, unmagnetized limit ($k_{\rm eff} \to 3/2$ as $\beta_0 \to \infty$, $R_{\rm B}/R_{\rm in} \to \infty$ and $\Re_{\rm B} \to \infty$). Moreover the form of the expression allows us to extrapolate, in the manner of Richardson extrapolation, to conditions we expect are relevant to Sgr A*: $\Re_{\rm B} \sim \infty$; $R_{\rm B}/R_{\rm in} \sim 10^5$ and $\beta_0 \sim 1{-}5$, then $k_{\rm eff} \sim 0.94$–1.0.

It is encouraging that this result lies in the vicinity of observational constraints, lending additional credence to the notion that Sgr A* is surrounded by a 'magnetically frustrated' accretion flow. We must recall, however, that this is only an extrapolation based on simulations which lack potentially important physics such as a relativistic inner boundary and a non-ideal plasma. The absence of an imposed outward convective luminosity is likely to be the essential element which allows for a lower value of k.

4 ROTATION MEASURE

The magnitude of RM constrains the density of the inner accretion flow, thereby also constraining the mass accretion rate and power-law index k. Future observations should provide time series of RM(t), a rich data set which encodes important additional information about the nature of the flow. Our goal in this section will be to characterize RM variability within our own simulations sufficiently well to distinguish them from other proposed flow classes.

We pause first to consider why RM should vary at all. The rotation of polarization is determined by an integral (equation A1, Shcherbakov 2008) which is proportional to $\int n_{\rm e}\boldsymbol{B}\,{\rm d}\boldsymbol{l}$ integrated over the zone of non-relativistic electrons. The integral is typically dominated by conditions at $R_{\rm rel}$, the radius where $kT_{\rm e} = m_{\rm e}c^2$. Even if $n_{\rm e}$ is reasonably constant, $\boldsymbol{B}$ likely will change in magnitude and direction as the flow evolves. Given that the dynamical time at $R_{\rm rel}$ is under a day, any strongly convective flow should exhibit significant day-to-day fluctuations in RM; measurements by Marrone et al. (2007) appear to rule this out. Rotational support also implies rapid RM fluctuations unless $\boldsymbol{B}$ is axisymmetric. In the highly subsonic flow of magnetically frustrated convection, however, RM may vary on much longer time-scales.

Two proposals have been advanced in which RM(t) would be roughly constant. Within their simulations of thick accretion discs, Sharma, Quataert & Stone (2007) show that trapping of poloidal flux lines leads to a rather steady value of RM for observers whose lines of sight are out of the disc plane. Sharma et al. (2008) point to the constancy of RM in the steady, radial magnetic configuration which develops due to the saturation of the magnetothermal instability (in the presence of anisotropic electron conduction). We suspect that noise at the dynamical frequency is to be expected in both these scenarios, which need not exist in a magnetically frustrated flow. We also note that both scenarios lead to systematically low values of RM for a given accretion rate, and therefore imply somewhat higher densities than we inferred from a spherical model; this may be observationally testable.

Our calculation of RM(t) is based on case 10 in Table 1. In Fig. 4 we plot RM(t) against an analytical estimate of its magnitude. For this purpose, we estimate RM as

$${\rm RM} \equiv \frac{e^3}{2\pi m_{\rm e}^2 c^4}\int_{R_{\rm rel}}^{R_{\rm B}} n_{\rm e}B\,{\rm d}r, \tag{7}$$

integrated along radial rays (two per coordinate axis) through the simulation volume. We neglect the difference between this expression and one which accounts for the relativistic nature of electrons within $R_{\rm rel}$. We therefore normalize RM to the estimate ${\rm RM}_{\rm est}$ as

$${\rm RM}_{\rm est} = \frac{e^3}{2c^4 m_{\rm e}^2}\left[\frac{GMR_{\rm rel}\mu_{\rm e}n_{\rm e}(R_{\rm rel})^3}{11\pi}\right]^{1/2}, \tag{8}$$

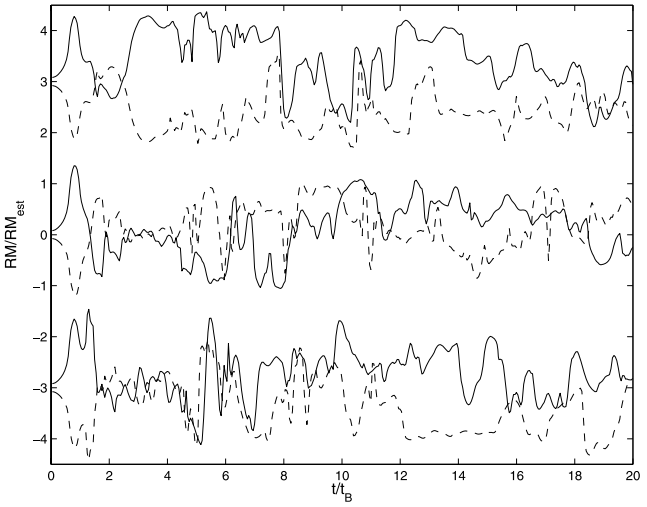

Figure 4. RM versus time (in units of $t_{\rm B}$). We chose $R_{\rm rel} = 17$, corresponding to $R_{\rm rel}/R_{\rm B} = 0.068$. Six lines represent three axes: upper set is X (centred at $+3$), centre is Y (centred at 0) and lower is Z (centred at -3), with positive and negative directions drawn as solid and dashed lines, respectively.

given by equation (A5) with $F(k, k_{\rm T}) \to 1$, $\langle\cos(\theta)\rangle \to 1/2$, $\beta \to 10$ and $k \to 1$. Because we do not calculate electron temperature within our simulations, we have the freedom to vary $R_{\rm rel}$ and to probe the dependence of coherence time on this parameter. In practice, we chose $R_{\rm rel} = (17, 26, 34, 43)\delta x_{\rm min}$ in order to separate this radius from the accretion zone ($7.5\delta x_{\rm min}$) and Bondi radius ($250\delta x_{\rm min}$, in this case). Fig. 4 illustrates RM(t) along each coordinate axis for the case with $R_{\rm rel} = 17\delta x_{\rm min}$). As this figure shows, RM changes slowly and its amplitude agrees with our estimate $\rm RM_{est}$. In our simulations, we can measure the full probability density function (PDF), shown in Fig. 5.

We can ask how well a single measurement of RM constrains the characteristic RM, say the ensemble-averaged rms value $\rm RM_{rms}$. This is a question of how well a standard deviation is measured from a single observation. From Fig. 5 we see that the distribution in our simulations is roughly Gaussian with standard deviation $\sigma_{\rm RM} = 0.63\rm RM_{est}$. One needs to apply Bayes' Theorem to infer the variance

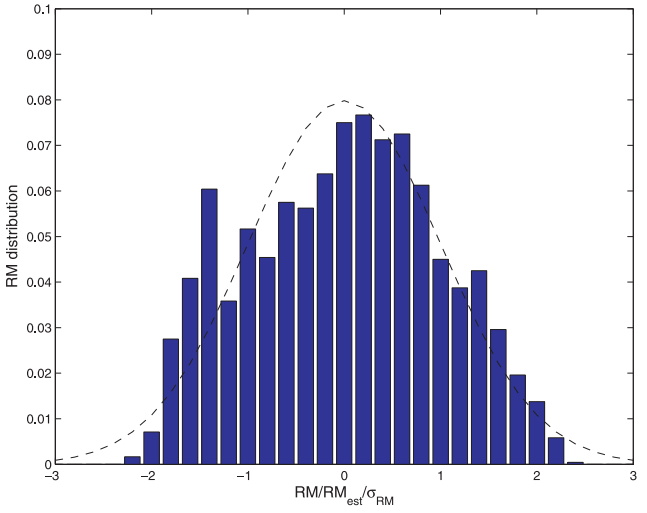

Figure 5. PDF of RM in Fig. 4. The dashed line represents a Gaussian distribution. The horizontal axis has been normalized by the standard deviation in Fig. 4, $\sigma_{\rm RM} = 0.63$.

of a Gaussian from N independent measurements:

$$\Delta\rm RM_{rms} = \left(\frac{2}{N}\right)^{1/2} \sigma_{\rm RM}. \tag{9}$$

To date, no sign change in RM has been observed, suggesting that we only have one independent measurement. Estimating $\rm RM_{rms}$ from a single data point requires a Bayesian inversion. Estimating from our simulation with a flat prior, the 95 per cent confidence interval for the ensemble characteristic RM given the one data point spans 2 orders of magnitude!

In other words, if in fact $\rm RM_{rms} = 5.4 \times 10^6$, it is not very surprising that we have observed $\rm RM \simeq -5.4 \times 10^5$. The maximum-likelihood estimate is $\rm RM_{rms} = RM$. The 95 per cent upper bound is $\rm RM_{rms} = 33RM$, and the lower bound is $\rm RM_{rms} = 0.33$ RM. More data are essential to constrain this very large uncertainty.

A visual description of the RM integrand through the flow is shown in Fig. 6. The time variability time-scale is shorter at small radii, and shorter at the beginning of the simulation. Simulations of many Bondi times with boundaries many Bondi radii away are necessary to see the characteristic flow patterns.

To be more quantitative, we plot in Fig. 7 the autocorrelation of RM(t) for different $R_{\rm rel}$. We define the coherence time τ to be the lag at which the autocorrelation of RM falls to 0.5.

The actual RM radius $R_{\rm rel}$ is not resolved in our simulations. In order to extrapolate to physically interesting regimes, we fit a trend to our limited dynamic range. The characteristic variability time-scale is given by the flow speed, so $\tau \propto R_{\rm rel}^3 \rho(R_{\rm rel})/\dot{M}$. For our characteristic values $k \sim 1$, we have $\tau \propto R_{\rm rel}^2$, which we fit to our coherence time, shown in Fig. 8.

For density profiles shallower than Bondi, the characteristic RM time-scale τ is significantly longer than the dynamical time [$\tau \sim (R_{\rm rel}/R_{\rm B})^{3/2} t_{\rm B}$]. In our fit, it is given by the accretion time:

$$\tau \sim 20 \left(\frac{R_{\rm rel}}{R_{\rm B}}\right)^2 \left(\frac{R_{\rm in}}{R_{\rm B}}\right)^{-1/2} t_{\rm B}, \tag{10}$$

with a relatively large dimensionless prefactor. This indicates a coherence time of order 1 yr for the conditions at Sgr A*. The actual value of $R_{\rm rel}$ is uncertain by a factor of 6, so the expected range could be from 2 months to 6 yr.

This is sufficiently distinct from one day that the distinction between frustrated and dynamical flows should be readily apparent, once observations span year-long baselines. We will discuss this point more in Section 5.1 below.

5 DISCUSSION

In this section we wish to revisit several of the physical processes which are missing from the current numerical simulations: stellar winds from within $R_{\rm B}$, the transport of energy and momentum by nearly collisionless electrons, and the inner boundary conditions imposed by a central black hole.

Stellar wind input. Our simulations account for the accretion of matter from outside the Bondi radius inferred from X-ray observations, but not for the direct input of matter from individual stars in the vicinity of the black hole. Loeb (2004) raises the possibility that individual stars may in fact dominate the accretion flow. The wind from a single star at radius r dominates the flow when its momentum output $\dot{M}_{\rm w} v_{\rm w}$ satisfies

$$\dot{M}_{\rm w} v_{\rm w} > 4\pi r^2 p(r) \to 3.3(10^{-5}\,{\rm M_\odot\,yr^{-1}})(1000\,{\rm km\,s^{-1}}), \tag{11}$$

where the evaluation is for a model consistent with RM constraints, in which density follows $n_{\rm H} \simeq 10^{7.3}(r/R_{\rm S})^{-1}\,{\rm cm^{-3}}$ and pressure

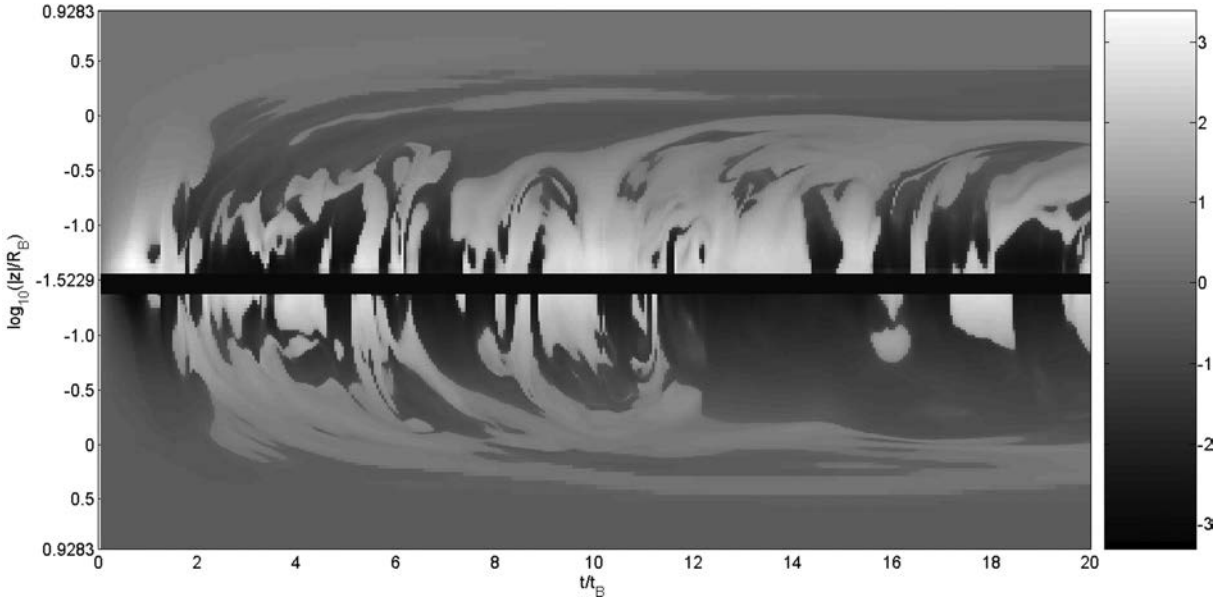

Figure 6. The RM integrant ρB_r versus radius and time. The central dark bar represents the inner boundary, the vertical axis is the Z-axis. The horizontal axis is time, in units of t_B; Grey-scale represents $\mathrm{sign}(B_r)\sqrt[4]{\rho|B_r|}$, which was scaled to be more visually accessible. The coherence time is longer at large radii and at late times. Several Bondi times are needed to achieve the steady state regime.

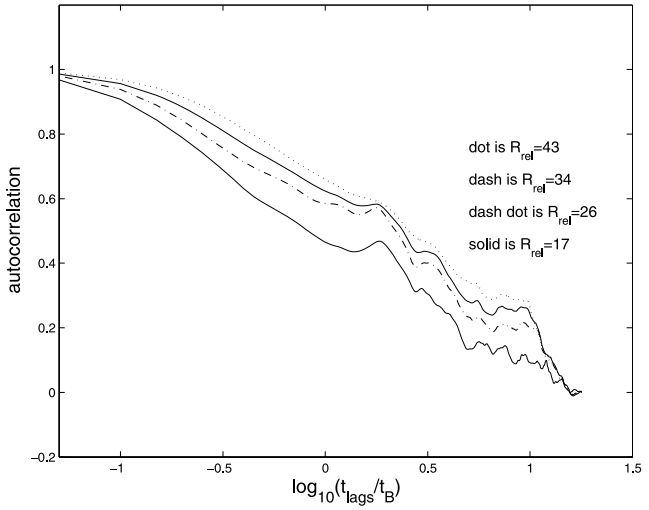

Figure 7. Autocorrelation for Fig. 4. X-axis represents time lags; Y-axis represents autocorrelation for different $R_{\rm in}$. The dotted, dashed, dot–dashed and solid lines correspond to $R_{\rm in} = 43$, 34, 26, 17, respectively.

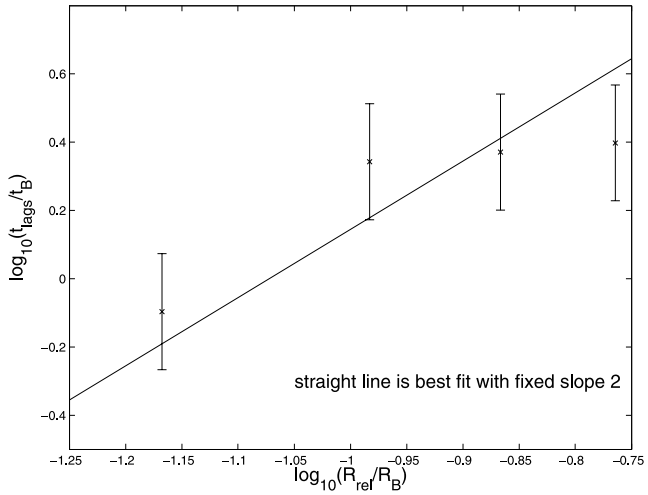

Figure 8. RM coherence time τ as a function of the inner truncation radius $R_{\rm rel}$; points refer to $R_{\rm rel} = 17$, 26, 34 and 43. The bootstrap error of 0.17 dex is based on the six data, two for each coordinate direction, at each $R_{\rm rel}$. The normalization for $R_{\rm rel} = R_{\rm B}$ is $\log_{10}(t_{\rm lags}/t_{\rm B}) = 2.15$.

follows $p \simeq 10^4 (r/R_{\rm S})^{-2}\,{\rm dyn\,cm^{-2}}$ – note that the criterion is independent of radius for $k = 1$. The required momentum output, equivalent to $10^{6.2}\,{\rm L}_\odot/c$, is well above the wind force of any of the OB stars observed within $R_{\rm B}$. While stars within $R_{\rm B}$ add fresh matter faster than it is accreted by the hole, we can be confident that no single star dominates the flow. If the density slope is substantially more shallow, for example in a CDAF with $k = 1/2$, the stellar winds would be a more important factor.

Collisionless transport. In the context of a dilute plasma where Coulomb collisions are rare, electron thermal conduction has the potential to profoundly alter the flow profile. The importance of this effect depends on the electrons' ability to freely stream down their temperature gradient (Sharma et al. 2008), despite the wandering and mirroring induced by an inhomogeneous magnetic field. The field must be weak for the magnetothermal instability to develop, yet weak fields are less resistive to tangling. The thermal conduction is expected to be strongest in the deep interior of the flow. If electrons actually free stream inside of 1000 Schwarzschild radii, the electrons could be non-relativistic all the way to the emission region, changing the interpretation of the RM. This would favour even shallower density profiles, for example the CDAF models. In such a model, the RM might be expected to vary on time-scales of minutes, which appears inconsistent with current data. If, on the other hand, the free streaming length is short on the inside, it more likely places the fluid in an ideal regime for the range of radii in our simulations. We therefore remain agnostic as to the role of thermal conduction in hot accretion flows, although it remains a primary caveat of the current study. Observations of time variability of RM will substantially improve our understanding.

Black hole inner boundary. Our current inner boundary conditions do not resemble a black hole very closely, apart from the fact that they also allow gas to accrete. As the inner region dominates the energetics of the flow, we consider it critical to learn how the black hole modifies our results. We are currently engaged in a follow-up study with a relativistic inner boundary, to be described in a future paper.

5.1 Observational probes

RM can be measured by several techniques. Currently, efforts have concentrated at high frequencies, $\nu \sim 200$–300 GHz (Marrone et al. 2006), where the polarization angle varies slowly with frequency. Accurate measurements over long time baselines allow discrimination between models. At high frequencies, the SMA and ALMA would allow a steady synaptic monitoring program. The full time series function extends the measurement space by one dimension.

At lower frequencies, high spectral resolution is needed to resolve the winding rate of polarization angle versus wavelength, which is now tractable with broad-band high-resolution instruments such as the EVLA and ATCA/CABB. The higher winding rate would allow a much more sensitive measurement of small changes in the RM, which would also be a discriminant between models. The challenge here is that the polarization fraction drops significantly with frequency, requiring a more accurate instrumental polarization model. On the other hand, the very characteristic λ^2 dependence of RM should allow a robust rejection against instrumental effects.

At lower frequency, the spatial extent of the emission region is also expected to increase. When the emission region approaches the RM screen, one expects depolarization. Direct polarized very long baseline interferometry imaging could shed light on this matter. This is complicated by interstellar scattering, which also increases the apparent angular size. The changing emission location as a function of frequency may complicate the RM inferences (Fish et al. 2009; Broderick & McKinney 2010). This can lead one to overestimate RM. The sign of RM would generically be a more robust quantity, and looking for changes in the sign of RM could be a proxy for the correlation function.

A separate approach is to use other polarized sources as probes of the flow. One candidate population is pulsars. At the Galactic Centre, interstellar scattering (Lazio & Cordes 2000) smears out the pulses, making them difficult to detect directly. However, the pulse averaged flux may itself be observable. Over the orbit around the black hole, one can measure the time variation of the RM, leading to a probe of the spatial RM variations in the accretion flow. Some pulsars, such as the Crab, exhibit giant pulses, which could still be visible despite a scattering delay smearing. These could be used to measure the dispersion measure along the orbit. The GMRT at 610 MHz would have optimal sensitivity to detecting the non-pulsating emission from pulsars, and be able to deconfuse them from the dominant synchrotron emission using RM synthesis (Brentjens & de Bruyn 2005).

6 CONCLUSION

A series of new, large dynamical range secular MHD simulation are presented for the understanding of the low luminosity of the supermassive black hole in the Galactic Centre. These are the first global 3D MHD simulations which do not face boundary conditions at outer radii, and impose ingoing boundaries at the interior, running for many Bondi times. We confirm a class of magnetically frustrated accretion flows, whose bulk properties are independent of physical and numerical parameters, including resolution, rotation and magnetic fields. Neither significant rotational support nor outward flow is observed in our simulations. An extrapolation formula is proposed and the accretion rate is consistent with observational data.

A promising probe for the nature of the accretion flow is the RM and its time variability. In this comparison, the dominant free parameter is the electron temperature. We argued that over the plausible range, from thermal to adiabatic, this radius varies from 40 to 250 Schwarzschild radii. The RM variations in the simulations are intermittent, requiring many measurements to determine this last free parameter.

We propose that temporal RM variations are a generic prediction to distinguish between the wide variety of theoretical models currently under consideration, ranging from CDAF through ADIOS to ADAF. RM is dominated by the radius at which electrons turn relativistic, when the flow is still very subrelativistic, and is thus much further out than the Schwarzschild radius. Most models, other than the ones found in our simulations, involve rapidly flowing plasmas, with Mach numbers near unity. These generically result in rapid RM variations on time-scales of hours to weeks (or in special cases, it can be infinite). In contrast, our simulations predict variability on time-scales of weeks to years. A major uncertainty in this prediction is the poor statistical measure of the standard deviation of RM measurement, which requires long-term RM monitoring to quantify.

Future observations of RM time variability, or spatially resolved measurements using pulsars, will provide valuable information.

ACKNOWLEDGMENTS

We would like to thank Avery Broderick, Ramesh Narayan, Roman Shcherbakov, Jim Stone, Mitch Begelman and Eliot Quataert for helpful discussions. This work was supported by the National Science and Engineering Research Council. The work of CDM was supported by Ontario ERA. The computations were performed on CITA's Sunnyvale clusters which are funded by the Canada Foundation for Innovation, the Ontario Innovation Trust and the Ontario Research Fund. The computations for the movies were performed on the GPC supercomputer at the SciNet HPC Consortium. SciNet is funded by the Canada Foundation for Innovation under the auspices of Compute Canada, the Government of Ontario, Ontario Research Fund – Research Excellence – and the University of Toronto.

REFERENCES

Agol E., 2000, ApJ, 538, L121
Baganoff F. K. et al., 2003, ApJ, 591, 891
Blandford R. D., Begelman M. C., 1999, MNRAS, 303, L1
Bondi H., 1952, MNRAS, 112, 195
Bower G. C., Backer D. C., Zhao J.-H., Goss M., Falcke H., 1999, ApJ, 521, 582
Brentjens M. A., de Bruyn A. G., 2005, A&A, 441, 1217
Broderick A. E., Blandford R. D., 2010, ApJ, 718, 1085
Broderick A. E., McKinney J. C., 2010, ApJ, 725, 750
Fish V. L., Doeleman S. S., Broderick A. E., Loeb A., Rogers A. E. E., 2009, ApJ, 706, 1353
Genzel R. et al., 2003, ApJ, 594, 812
Gillessen S., Eisenhauer F., Trippe S., Alexander T., Genzel R., Martins F., Ott T., 2009, ApJ, 692, 1075
Gruzinov A., 2001, preprint (astro-ph/0104113)
Igumenshchev I. V., Narayan R., 2002, ApJ, 566, 137
Igumenshchev I. V., Narayan R., Abramowicz M. A., 2003, ApJ, 592, 1042
Johnson B. M., Quataert E., 2007, ApJ, 660, 1273

Kaeppeli R., Whitehouse S. C., Scheidegger S., Pen U. L., Liebendoerfer M., 2009, preprint (arXiv:0910.2854)
Lazio T. J. W., Cordes J. M., 2000, in Kramer M., Wex N., Wielebinski R., ASP Conf. Ser. Vol. 202, IAU Colloq. 177, Pulsar Astronomy – 2000 and Beyond. Astron. Soc. Pac., San Francisco, p. 39
Levin Y., Beloborodov A. M., 2003, ApJ, 590, L33
Loeb A., 2004, MNRAS, 350, 725
Marrone D. P., Moran J. M., Zhao J.-H., Rao R., 2006, J. Phys. Conf. Ser., 54, 354
Marrone D. P., Moran J. M., Zhao J.-H., Rao R., 2007, ApJ, 654, L57
Narayan R., Yi I., 1994, ApJ, 428, L13
Narayan R., Igumenshchev I. V., Abramowicz M. A., 2000, ApJ, 539, 798
Pang B., Pen U., Perrone M., 2010, preprint (arXiv e-prints)
Pen U.-L., Arras P., Wong S., 2003a, ApJS, 149, 447
Pen U.-L., Matzner C. D., Wong S., 2003b, ApJ, 596, L207
Proga D., Begelman M. C., 2003, ApJ, 592, 767
Quataert E., Gruzinov A., 2000a, ApJ, 545, 842
Quataert E., Gruzinov A., 2000b, ApJ, 539, 809
Quataert E., Narayan R., 1999, ApJ, 520, 298
Revnivtsev M. G. et al., 2004, A&A, 425, L49
Sharma P., Quataert E., Stone J. M., 2007, ApJ, 671, 1696
Sharma P., Quataert E., Stone J. M., 2008, MNRAS, 389, 1815
Shcherbakov R. V., 2008, ApJ, 688, 695
Shcherbakov R. V., Baganoff F. K., 2010, ApJ, 716, 504
Tanaka T., Menou K., 2006, ApJ, 649, 345
Yuan F., Quataert E., Narayan R., 2003, ApJ, 598, 301
Yusef-Zadeh F., Muno M., Wardle M., Lis D. C., 2007, ApJ, 656, 847
Yusef-Zadeh F. et al., 2009a, ApJ, 706, 348
Yusef-Zadeh F. et al., 2009b, ApJ, 702, 178

APPENDIX A: ROTATION MEASURE CONSTRAINT ON ACCRETION FLOW

In traversing the accretion flow, linearly polarized radio waves of wavelength λ are rotated by RM λ^2 radians, where

$$\mathrm{RM} = \frac{e^3}{2\pi m_\mathrm{e}^2 c^4} \int n_\mathrm{e} f(T_\mathrm{e}) B \cos(\theta)\, \mathrm{d}l. \tag{A1}$$

Here $f(T_\mathrm{e})$ is a ratio of modified Bessel functions: $f(T_\mathrm{e}) = K_0(m_\mathrm{e}c^2/k_\mathrm{B}T_\mathrm{e})/K_2(m_\mathrm{e}c^2/k_\mathrm{B}T_\mathrm{e})$ (Shcherbakov 2008), which suppresses RM by a factor $\propto T_\mathrm{e}^{-2}$ wherever electrons are relativistic. The integral here covers the entire path from source to observer; θ is the angle between $\boldsymbol{B}$ and the line of sight. This expression is appropriate for the frequencies at which RM has been observed; at lower frequencies, where propagation is 'superadiabatic' (Broderick & Blandford 2010) $\cos(\theta) \rightarrow \pm|\cos(\theta)|$.

We adopt a power-law solution with negligible rotational support in which $\rho \propto r^{-k}$, and the total pressure $P \propto r^{-k_P}$ with $k_P = k + 1$; moreover we take $T_\mathrm{e} \propto r^{-k_\mathrm{T}}$ for the relativistic electrons. The hydrostatic equation $\mathrm{d}P/\mathrm{d}r = -GM\rho/r^2$ becomes

$$P = P_\mathrm{g} + P_\mathrm{B} = \frac{GM}{(k+1)}\frac{\rho}{r}, \tag{A2}$$

and with $P_\mathrm{g} = \beta P_\mathrm{B} = \beta B^2/(8\pi)$, $\rho = n_\mathrm{e}\mu_\mathrm{e}$ (where $\mu_\mathrm{e} = 1.2m_\mathrm{p}$ is the mass per electron),

$$B = \left[\frac{8\pi}{(\beta+1)(k+1)}\frac{GM\mu_\mathrm{e}n_\mathrm{e}}{r}\right]^{1/2}. \tag{A3}$$

So long as $k > 1/3$ (so that RM converges at large radii) and $k < (1 + 4k_\mathrm{T})/3$ (so it converges inward as well), the RM integral is set around R_rel. Taking a radial line of sight ($\mathrm{d}l \rightarrow \mathrm{d}r$), we write

$$\int_0^\infty n_\mathrm{e} f(T_\mathrm{e}) B\cos(\theta)\,\mathrm{d}r = F(k,k_\mathrm{T})\int_{R_\mathrm{rel}}^\infty n_\mathrm{e} B\cos(\theta)\,\mathrm{d}r = \frac{2}{3k-1}\langle\cos(\theta)\rangle F(k,k_\mathrm{T})\,[n_\mathrm{e}Br]_{R_\mathrm{rel}}, \tag{A4}$$

where $\langle\cos(\theta)\rangle$ encapsulates the difference between the true integral what it would have been if $\theta = 0$ all along the path, and $F(k, k_\mathrm{T})$ encapsulates the difference between a smooth cut-off and a sharp one. We plot $F(k, k_\mathrm{T})$ in Fig. A1; it is of order unity except as k_T approaches $(3k - 1)/4$. All together,

$$\mathrm{RM} = \frac{4e^2\,GM}{m_\mathrm{e}^2c^5}\frac{\langle\cos(\theta)\rangle F(k,k_\mathrm{T})}{3k-1}\left[\frac{\mu_\mathrm{e}n_\mathrm{e}(R_\mathrm{rel})^3}{\pi(k+1)(\beta+1)}\frac{R_\mathrm{rel}}{R_\mathrm{S}}\right]^{1/2}. \tag{A5}$$

To estimate $n_\mathrm{e}(R_\mathrm{rel})$ from RM, one must make assumptions about the uncertain parameters β, $\langle\cos(\theta)\rangle$, k_T and $R_\mathrm{rel}/R_\mathrm{S}$; then k can be derived self-consistently from observations $n_\mathrm{e}(R_\mathrm{B})$ and RM. Our fiducial values of these parameters are 10, 0.5, 0.5 and 100, respectively, of which we consider the last to be the most uncertain. We now discuss each in turn.

Although the magnetization parameter β could conceivably take a very wide range of values, we consistently find $\beta \simeq 10$ in our simulations, with some tendency for β to decrease inward. We consider it unlikely for the flow to be much less magnetized, given the magnetization of the galactic centre and the fact that weak fields are enhanced in most of the flow models under consideration.

If $\boldsymbol{B}$ wanders little in the region where the integrand is large (a zone of width $\sim R_\mathrm{rel}$ around R_rel), and is randomly oriented relative to the line of sight $\langle\cos(\theta)\rangle \simeq \cos[\theta(R_\mathrm{rel})]$, typically 1/2 in absolute value. If the field were purely radial, $\langle\cos(\theta)\rangle$ would be unity. Conversely, if $\boldsymbol{B}$ reverses frequently in this region (the number of reversals N_r is large) then $\langle\cos(\theta)\rangle_\mathrm{rms} \simeq 1/(2\sqrt{N_\mathrm{r}+1})$ will be small. However, N_r cannot be too large, or magnetic forces are unbalanced. We gauge its maximum value by equating the square of the buoyant growth rate, $\mathcal{N}^2 = [(3-2k)/5]GM/r^3$, against the square of the Alfvén frequency $N_\mathrm{r}^2 v_\mathrm{A}^2/r^2$. Noting that

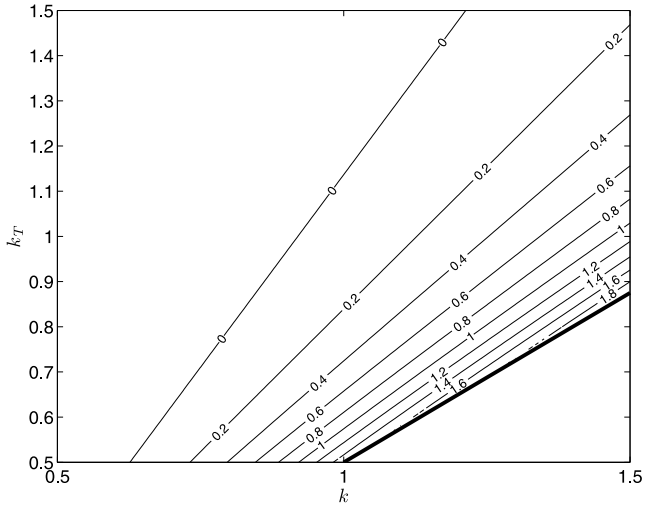

Figure A1. The logarithm of the relativistic RM factor, $\log_{10}F(k, k_\mathrm{T})$. The true RM integral is modified by a factor $F(k, k_\mathrm{T})$ relative to an estimate in which the non-relativistic formula is used, but the inner bound of integration is set to the radius R_rel at which electrons become relativistic; see equation (A1).

$v_A^2 = GM/[2(\beta+1)(k+1)r]$, we find $N_r^2 \simeq (2/5)(\beta+1)(k+1)(3-2k)$. For $\beta = 10$ and $k = 1$, this implies $\langle\cos(\theta)\rangle_{rms} \simeq 0.25$, a very minor suppression. We can therefore be confident that $\langle\cos(\theta)\rangle = 0.5$ to within a factor of 2, unless $\beta \gg 10$ for some reason.

The precise value of k_T is not important unless it approaches or falls below the minimum value $(3k-1)/4$. If electron conduction is very strong this is unavoidable, as rapid transport implies $k_T \simeq 0$; however in this case the relativistic region disappears, as discussed below. Alternately, if relativistic electrons are trapped and adiabatic, $T_e \propto \rho^{1/3}$ and $k_T = k/3$; however $k_T < (3k-1)/4$ then requires $k < 3/5$, which can only be realized within the CDAF model. Finally, if electrons remain strongly coupled to ions, $k_T = 1$ and we only require $k < 5/3$.

The location at which electrons become relativistic, R_{rel}, is quite uncertain. Models such as those of Yuan, Quataert & Narayan (2003), in which electrons are heated while advecting inward, predict $R_{rel} \simeq 10^2 R_S$. The maximum conceivable R_{rel} corresponds to adiabatic compression of the electrons, inward from the radius at which they decouple from ions; this yields about $500/(1+k)R_S$. If conduction is very strong, however, electrons should remain cold throughout the flow; in this case we should replace $R_{rel}/R_S \to 1$ and $F(k, k_T) \to 1$ in equation (A5).

Adopting our fiducial values for the other variables, and taking $F(k, k_T) \to 1$ for lack of knowledge regarding k_T, we may solve for the self-consistent value of k which connects the density at R_B with $n_e(R_{rel})$ derived from equation (A5). We find $k \to$ (0.90, 1.23, 1.32) for $R_{rel}/R_S \to$ (200, 100, 1), respectively. As noted in the text, the current small set of RM measurements allows a 2 order of magnitude range in RM_{est}, and $k \sim 1$ is consistent with data. Longer observations of time and amplitude will improve the constraints.

APPENDIX B: INNER BOUNDARY CONDITIONS

The inner boundary conditions were determined by first solving for the vacuum solution of the magnetic field inside the entire inner boundary cube. Then inside the largest possible sphere within this cube, matter and energy were removed.

To simplify the programming, we put the entire inner boundary region on one node. This meant that the grid had to be divided over an odd number of nodes in each Cartesian direction.

B1 Magnetic field

In order to determine the vacuum magnetic field solution, we use the following two Maxwell equations for zero current:

$$\nabla \cdot \boldsymbol{B} = 0, \tag{B1}$$

$$\nabla \times \boldsymbol{B} = 0. \tag{B2}$$

Equation (B2) enables us to write $\boldsymbol{B} = \nabla\phi$, for some scalar function ϕ. Combining this with (B1) we obtain Laplace's equation:

$$\nabla^2\phi = 0, \tag{B3}$$

which we solve with Neumann boundary conditions (the normal derivative $\hat{\boldsymbol{n}} \cdot \nabla\phi$ specified) given by $\boldsymbol{B} \cdot \hat{\boldsymbol{n}}$ on the boundary of the cube.

Since the MHD code stores the values of $\boldsymbol{B}$ on the left-hand cell faces, we must solve for ϕ in cell centres and then take derivatives to get the value of $\boldsymbol{B}$ on the cell boundary. Let the inner boundary cube be of side length N, consisting of cells numbered $1, \ldots, N$ in all three directions. In order to simplify the problem, we set $\boldsymbol{B} \cdot \hat{\boldsymbol{n}} = 0$ on five of the six faces of the cube, and find the contribution to ϕ from one face at a time.

Suppose $\boldsymbol{B} \cdot \hat{\boldsymbol{n}} = 0$ on all of the faces except the $i = N+1$ face (i.e., $B_x^{N+1,j,k}$ can be non-zero). The Laplace equation (B3) with Neumann boundary conditions only has a solution if the net flux of field into the cube is zero. Since all of the boundary conditions are zero except for the $i = N+1$ face, that face must have a net flux through it of zero. Defining

$$\overline{B_x^{N+1}} = \frac{1}{N^2}\sum_{j=1}^{N}\sum_{k=1}^{N} B_x^{N+1,j,k} \tag{B4}$$

to be the average of B_x on the $i = N+1$ face, and letting $b_x^{N+1,j,k} = B_x^{N+1,j,k} - \overline{B_x^{N+1}}$, $b_x^{N+1,j,k}$ can be used as the boundary condition and $\overline{B_x^{N+1}}$ will be added in later.

We use separation of variables to solve for ϕ. Set $\phi^{ijk} = X^i Y^j Z^k$, substitute into (B3), and rearrange to get

$$\frac{X^{i+1} - 2X^i + X^{i-1}}{X^i} + \frac{Y^{j+1} - 2Y^j + Y^{j-1}}{Y^j} + \frac{Z^{k+1} - 2Z^k + Z^{k-1}}{Z^k} = 0. \tag{B5}$$

Now let

$$\frac{Y^{j+1} - 2Y^j + Y^{j-1}}{Y^j} = -\eta^2, \quad \text{and} \tag{B6}$$

$$\frac{Z^{k+1} - 2Z^k + Z^{k-1}}{Z^k} = -\omega^2. \tag{B7}$$

Solving equations (B6) and (B7) with the boundary conditions,

$$Y_m^j = \cos\frac{m\pi\left(j-\frac{1}{2}\right)}{N}, \qquad Z_n^k = \cos\frac{n\pi\left(k-\frac{1}{2}\right)}{N}, \tag{B8}$$

$$\eta_m^2 = 4\sin^2\frac{m\pi}{2N}, \qquad \omega_n^2 = 4\sin^2\frac{n\pi}{2N}. \tag{B9}$$

Substituting (B6), (B7) and (B9) into (B5), and solving, yields

$$X_{mn}^i = \cosh\frac{\alpha_{mn}\pi\left(i-\frac{1}{2}\right)}{2N}, \tag{B10}$$

where

$$\alpha_{mn} = \frac{2N}{\pi}\operatorname{arcsinh}\sqrt{\sin^2\frac{n\pi}{2N} + \sin^2\frac{m\pi}{2N}}. \tag{B11}$$

Finally, putting this all together,

$$\phi^{ijk} = \sum_{m=0}^{N-1}\sum_{n=0}^{N-1} A_{mn}\cos\frac{m\pi\left(j-\frac{1}{2}\right)}{N}\cos\frac{n\pi\left(k-\frac{1}{2}\right)}{N} \times \cosh\frac{\alpha_{mn}\pi\left(i-\frac{1}{2}\right)}{N}, \tag{B12}$$

and define $A_{00} = 0$.

To determine the coefficients A_{mn} we add in the final boundary condition ($i = N+1$), and get

$$A_{mn} = \frac{4}{N^2}\frac{1}{2\sinh(\alpha_{mn}\pi)\sinh(\alpha_{mn}\pi/2N)} \times \sum_{j=1}^{N}\sum_{k=1}^{N} b_x^{N+1,j,k}\cos\frac{m\pi(j-\frac{1}{2})}{N} \times \cos\frac{n\pi\left(k-\frac{1}{2}\right)}{N}. \tag{B13}$$

A similar calculation may be performed for the case when the $i = 1$ boundary has non-zero field. After finding the contribution from each face, we store their sum in ϕ.

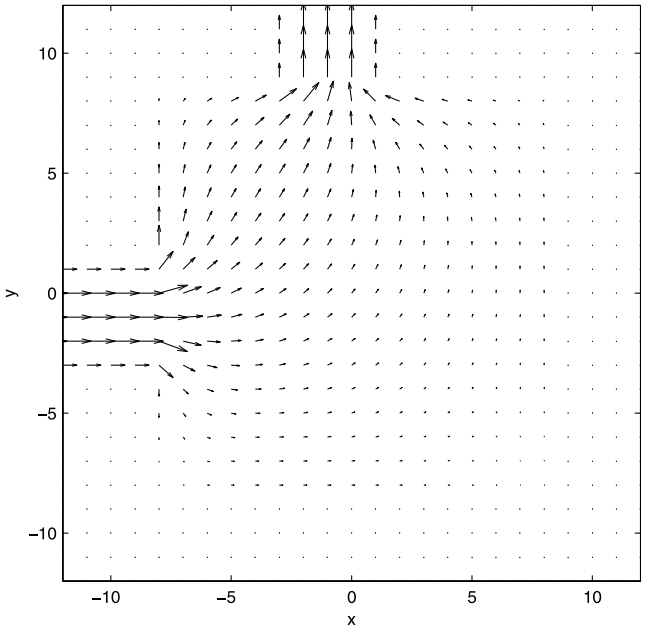

Figure B1. Vacuum solution of the magnetic field is calculated in the central region. The field lines outside of the central region show the boundary condition.

To deal with the subtracted cube face field averages, let

$$\phi_0^{ijk} = \overline{B_x^{1jk}}\,i + \overline{B_y^{i1k}}\,j + \overline{B_z^{ij1}}\,k + \frac{\overline{B_x^{N+1,j,k}} - \overline{B_x^{1jk}}}{2N}(i^2 + j^2) + \frac{\overline{B_x^{N+1,j,k}} + \overline{B_y^{i,N+1,k}} - \overline{B_x^{1jk}} - \overline{B_y^{i1k}}}{2N}(j^2 + k^2), \quad \text{(B14)}$$

and add this to ϕ. ϕ_0 is the potential of a cube where each face has the uniform magnetic field given by the average of the magnetic field on the corresponding face of the inner boundary cube.

To find $\boldsymbol{B}$, we set

$$B_x^{ijk} = \phi^{ijk} - \phi^{i-1,j,k}, \quad \text{(B15)}$$

$$B_y^{ijk} = \phi^{ijk} - \phi^{i,j-1,k}, \quad \text{(B16)}$$

$$B_z^{ijk} = \phi^{ijk} - \phi^{i,j,k-1}. \quad \text{(B17)}$$

In Fig. B1 we used the magnetic field solver with a boundary condition consisting of field going in one side and out an adjacent side of the box. This boundary condition tests both the ϕ_0 component of the solution (since faces have non-zero net flux) as well as the Fourier series component (since faces have non-constant magnetic field).

B2 Density and pressure

Inside the largest possible sphere that can be inscribed within the inner boundary cube, we adjust the density and pressure so that the Alfvén speed and the sound speed are both equal to the circular speed. We accomplish this by setting

$$\rho = \frac{\boldsymbol{B}^2 r}{GM_{\rm BH}}, \quad \text{(B18)}$$

$$p = \frac{GM_{\rm BH}\rho}{r\gamma}. \quad \text{(B19)}$$

We then set p to $0.1p$. ρ and p were assigned minimum values of 0.1 times the average value of ρ outside of the sphere, and 0.001, respectively, to ensure stability.

APPENDIX C: ANIMATION OF MAGNETICALLY FRUSTRATED CONVECTION SIMULATION

The qualitative behaviour of the accretion flow is best illustrated in the form of a movie, available as Supporting Information with the electronic version of the article. This movie shows case 25. The raw simulation used 600^3 grid cells. The Bondi radius is at 1000 grid units, where one grid unit is the smallest central grid spacing. The full box size is 8000^3 grid units. Colour represents the entropy, and arrows represent the magnetic field vector. The right-hand side shows the equatorial plane (yz), the left-hand side shows a perpendicular plane (xy). The moving white circles represent the flow of an unmagnetized Bondi solution, starting at the Bondi radius. On average, the fluid is slowly moving inward, in a state of magnetically frustrated convection. Various other formats can also be seen at http://www.cita.utoronto.ca/pen/MFAF/blackhole_movie/index.html.

SUPPORTING INFORMATION

Additional Supporting Information may be found in the online version of this article:

Movie C1. Animation of magnetically frustrated convection simulation.

Please note: Wiley-Blackwell are not responsible for the content or functionality of any supporting materials supplied by the authors. Any queries (other than missing material) should be directed to the corresponding author for the article.

This paper has been typeset from a TEX/LATEX file prepared by the author.